https://doi.org/10.5194/egusphere-2024-532
Preprint. Discussion started: 8 March 2024

How Many Parameters are Needed to Represent Polar Sea Ice Surface Patterns and Heterogeneity?

Joseph Fogarty[1], Elie Bou-Zeid[1], Mitchell Bushuk[2], and Linette Boisvert[3]

[1]Civil and Environmental Engineering Department, Princeton University, Princeton NJ, USA
[2]National Oceanic and Atmospheric Administration, Geophysical Fluid Dynamics Laboratory, Princeton NJ, USA
[3]Cryospheric Sciences Lab, NASA Goddard Space Flight Center, Greenbelt MA, USA

Correspondence: Joseph Fogarty (jf38@princeton.edu)

Abstract. Sea ice surface patterns encode more information than can be represented solely by the ice fraction. The aim of this paper is thus to establish the importance of using a broader set of surface characterization metrics, and to identify a minimal set of such metrics that may be useful for representing sea-ice in Earth System Models. Large-eddy simulations of the atmospheric boundary layer over various idealized sea ice surface patterns, with equivalent ice fraction and average floe area, demonstrate that the spatial organization of ice and water can play a crucial role in determining boundary-layer structure. Thus, different methods to quantify heterogeneity in categorical lattice spatial data, such as those done in landscape ecology and Geographic Information System (GIS) studies, are used here on a set of high-resolution, recently-declassified sea ice surface images. It is found that, in conjunction with ice fraction, the patch density (representing the fragmentation of the surface), the splitting index (representing the variability in patch size), and perimeter-area fractal dimension (representing the tortuosity of the interface) are all required to describe the two-dimensional pattern exhibited by a sea ice surface. Furthermore, for surfaces with anisotropic patterns, the orientation of the surface relative to the mean wind is needed. Furthermore, scaling laws are derived for these relevant landscape metrics to estimate them from aggregated spatial sea ice surface data at any resolution. The methods used and results gained from this study are a first step towards further development of methods to quantify the variability of non-binary surfaces, and for parameterizing mixed ice-water surfaces in coarse geophysical models.

1 Introduction

The polar sea ice surface, a sensitive indicator of global climate change, shows persistent biases in coarse-resolution Earth System Model (ESMs) (Liu et al., 2022; Casagrande et al., 2023; Myksvoll et al., 2023). Among other causes, these biases result from the inability of ESMs to resolve the fine-scale spatial variability of sea ice, and the resulting exchanges with the ocean below (Ramudu et al., 2018) and atmosphere aloft (Bates et al., 2006; Esau, 2007). The effect of this subgrid scale sea ice variability is typically parameterized in climate models using the ice fraction, f_i, to determine surface-atmosphere fluxes for an equivalent surface that would produce the same grid-cell averaged exchanges as the ice-water mixture. Usually, either an equivalent homogeneous surface or mosaic flux aggregation are used (Bou-Zeid et al., 2020), but both yield an average flux weighted by the ice and water fractions that is inaccurate as it does not account for the impact of surface heterogeneity on the dynamics of the lower atmosphere and the nonlinear interactions with the air flow above the ice and water (de Vrese et al.,

https://doi.org/10.5194/egusphere-2024-532
Preprint. Discussion started: 8 March 2024

2016). This incomplete representation of sea ice surface and boundary-layer structure then results in errors in the turbulent exchanges of heat, moisture, and momentum across polar sea ice surface (Nilsson et al., 2001; Bourassa et al., 2013; Taylor et al., 2018). The dynamics and secondary circulations below the first vertical grid cell level in climate models are particularly under-resolved, and they have a direct impact on air-surfaces exchanges; it thus are imperative to understand how these features influence fluxes (Mahrt, 2000; Essery et al., 2003; de Vrese et al., 2016). These gaps in representing fine scale dynamics and fluxes propagate to the projection of future changes in the Arctic climate system and resulting surface energy budget (Persson et al., 2002; Miller et al., 2017). which may be one reason why climate model ensembles consistently underpredict Arctic sea ice sensitivity to surface temperature warming. This underprediction has persisted throughout the last three Intergovernmental Panel on Climate Change (IPCC) model development cycles (Stroeve et al., 2007; Rosenblum and Eisenman, 2016, 2017; Notz and Community, 2020). The resulting uncertainty in climate models' ability to predict sea ice future evolution hinders effective action and decision-making; therefore, improving these models is more imperative now than ever (Notz and Stroeve, 2018; Docquier and Koenigk, 2021).

The fringe zone that separates densely consolidated sea ice from the open ocean is known as the marginal ice zone (MIZ) (Dumont, 2022). In the MIZ, the sizes and organization of sea ice floes and water are influenced by winds, sea currents, waves, and material ice properties (Wang et al., 2016; Ren et al., 2021; Herman et al., 2021; Hwang and Wang, 2022). What makes this region unique is that the near-surface air temperatures may fall in between the surface temperatures of the sea ice and water, resulting in abrupt spatial transitions between stabilizing and destabilizing surface buoyancy fluxes. Such transitions produce drastically different turbulence-mean non-equilibrium dynamics and time scales (as show for comparable land-water transitions by Allouche et al. (2021)), all affecting the surface-atmosphere exchanges between the air, water, and sea ice. The ice fraction f_i in the MIZ is between 15% and 80% (Strong et al., 2017); however, any region of fractured sea ice gives rise to these abrupt transitions. It is precisely in these regions where the linear weighted averaged approaches described above will be most inadequate, and where the surface transitions will play a key role in the dynamics. Thus, it is important to devise better methods to quantify the heterogeneity of a surface, characterize its patterns, and represent this information in coarse-resolution ESMs to better represent the polar environment.

To that end, the complex geometric patterns formed by sea ice floes need to be analyzed. Larger floes will have proportionally more of an effect on the surface-atmosphere fluxes, but smaller floes, with more frequent transitions, will exacerbate the non-linearity of the exchange processes. These surface-atmosphere fluxes impart a large effect on the atmospheric boundary layer (ABL) overlaying the marginal ice zone (MIZ-ABL). As a thought experiment, consider an ice-water surface with a very fine checkerboard pattern, and a sea ice fraction of $f_i = 0.5$; this configuration will lead to statistically-homogeneous ice floes that are locally variable at the surface, but are effectively homogeneous in regards to the MIZ-ABL where turbulence will rapidly mix their small-scale signatures (Brutsaert, 2005; Mahrt, 2000; Bou-Zeid et al., 2004). However, two large patches of sea ice and water (meso-α heterogeneity, see Bou-Zeid et al. (2020)), also with a sea ice fraction of $f_i = 0.5$, will develop a large circulation closer to that of a sea breeze due to the abrupt transition between two large homogeneous surfaces (Porson et al., 2007; Crosman and Horel, 2010; Allouche et al., 2023). The dynamics and thermodynamics in this MIZ-ABL system, and

https://doi.org/10.5194/egusphere-2024-532
Preprint. Discussion started: 8 March 2024

the surface exchange therein, will thus be quite different over these two patterns even if the some key surface properties, e.g. temperature and roughness, are identical (Bou-Zeid et al., 2007).

Given its importance and the challenges outlined above, previous work has attempted to quantify the heterogeneity of sea ice surfaces (Wenta and Herman, 2018, 2019; Michaelis et al., 2020; Horvat, 2021; Dumont, 2022) utilizing surface and meteorological properties such as sea ice fraction, geostrophic velocity, lead width, or floe size distribution. However, the small-scale patterns in the MIZ, especially as the resolution is increased, require broader and more versatile methods of heterogeneity characterization (e.g., Mandelbrot (1967)). In addition, the computational grid of even the highest-resolution numerical models cannot resolve all the spatial features in the MIZ. One thus needs to consider how to represent surface characteristics in model grids that can be thought of as lattice-type spatial structures, defined by Cressie (1993). Observational data of MIZ ice patterns also have a finite resolution and are thus comparable to lattice data, which then allows one to utilize different metrics specifically defined for lattice surfaces that offer ways to characterize the heterogeneity patterns of these surfaces. In this paper, we examine approaches for this quantification commonly used in landscape ecology, a field that has generated a multitude of ways to study lattice spatial data (Li and Reynolds, 1994, 1995; Pickett and Cadenasso, 1995).

Studies in landscape ecology have previously searched for an optimal independent group of metrics to be used in understanding the heterogeneity of lattice surfaces. Riitters et al. (1995) used a multivariate factor analysis to suggest six groups of metrics, including image texture, average pact compaction, and average patch shape. Cushman et al. (2008) used principal component analysis to suggest seven broad metrics at the landscape level, including contagion, large patch dominance, and proximity (see Table 9 in that study). For the two-dimensional binary sea ice-water surfaces considered in this study, we chose the variance inflation factor (VIF) technique to reduce these metrics to a compact set that are weakly dependent on one another to minimize information redundancy (Miles, 2014).

The questions that will be answered in this study are:

1. Is the sea ice fraction of a MIZ surface, combined with some measure of average floe area, sufficient to predict the behavior of the overlying MIZ-ABL?
2. If not, what other surface information in a two-dimensional lattice spatial pattern is needed to describe air-sea interaction?
3. How can this surface information be applied to sea ice surfaces in weather models and ESMs, considering factors such as availability of information, resolution-resampling invariance, and ease of understanding?

Section 2 will detail the methods on the idealized and real-world maps used in this study; this includes the steps taken to reduce multicolinearity and determine which landscape metrics, alongside sea ice fraction, give additional information on the pattern of the sea-ice surface. The large-eddy simulations that will be used are also presented in this section, but a more complete description is found in Appendices A and B. Section 3 will report the results of the idealized sea ice surfaces in the large-eddy simulation, thus answering Question 1. Section 4 will report the results from the 2D surface analysis, with additional discussion in Section 5 on principal directions and climate model implications, thus answering Questions 2 and 3. Section 6 will synthesize the findings and outline open questions that can guide future investigations of sea ice heterogeneity.

https://doi.org/10.5194/egusphere-2024-532
Preprint. Discussion started: 8 March 2024

Table 1. Large-eddy simulation numerical details. Time is represented in terms of inertial periods, $2\pi/f_c$, which is the time scale associated with the response of the mean flow since it represents the Coriolis redistribution of energy between u and v (Momen and Bou-Zeid, 2016)

Domain height, z_i	$1\,\mathrm{km}$
Horizontal domain size, $L_x \times L_y$	$10\,\mathrm{km} \times 10\,\mathrm{km}$
Number of grid points (N_x, N_y, N_z)	$(100, 100, 50) \approx 5 \times 10^5$ points
Vertical mesh spacing, dz	$20\,\mathrm{m}$
Horizontal mesh spacing, dx, dy	$100\,\mathrm{m}$
Initial air temperature $\theta_{a,0}$	See Appendix B, constant profile
Warm up period	5 inertial periods $(10\pi/f_c)$
Simulation time step	$0.05\,\mathrm{s}$
Averaging period	1 inertial period $(2\pi/f_c)$
Frequency of statistical sampling	100 timesteps = $5\,\mathrm{s}$

2 Methods and Data

2.1 Large-Eddy Simulations

Large-eddy simulations (LES) are widely used to model heterogeneous high Reynolds number flows (Baidya Roy, 2002; Bou-Zeid et al., 2004) in convective boundary layers (Courault et al., 2007; Maronga and Raasch, 2013), stable boundary layers (Huang et al., 2011), and coastlines (Allouche et al., 2023) to name a few; see Section 3.6 of Stoll et al. (2020). This heterogeneous high-Reynolds number description aptly applies to the MIZ-ABL. Unlike a direct numerical simulation (DNS), an LES is able to attain Reynolds numbers representative of the MIZ-ABL (Re $\sim 10^7$), because the smaller turbulent eddies (smaller than the grid or filter size, which is comparable to the numerical grid spacing in our simulations) are not explicitly resolved. However, unlike Reynolds averaged Navier-Stokes (RANS) approaches, which encompass all weather and climate models, LES directly resolves and captures the large turbulent eddies, the heterogeneity of the surface, advective fluxes, and the large-scale sea ice patterns, making it a computationally and physically appealing approach for the problem at hand. By retaining these larger structures, most of the turbulent energy and fluxes are explicitly resolved, allowing for investigation of three-dimensional flow structures that may arise over these heterogeneous surfaces.

LES is thus used to model MIZ-ABL flow over 10 km $\times$ 10 km patterns of idealized ice/water surfaces, modulated by a Coriolis force at the latitude of $\Phi = 90°$ N. This full domain is smaller than a single grid cell in state-of-the-art ESMs, underlining why the simulated properties of the MIZ-ABL in ESMs require sub-grid scale (SGS) parameterization. More details on the numerical aspects of our LES are described in Appendix A. For the bottom boundary condition, one surface node represents either water or sea ice, as done in Fogarty and Bou-Zeid (2023). This bottom boundary for each simulation can be thought of as categorical lattice spatial data, where each node represents either "ice" or "water." An "ice" node is prescribed a surface temperature of $255\,\mathrm{K}$, typical of autumn and spring temperatures in the Central Arctic, and a momentum roughness

https://doi.org/10.5194/egusphere-2024-532
Preprint. Discussion started: 8 March 2024

length of 1 mm, while a "water" node is prescribed a surface temperature of 271 K, roughly the freezing point of seawater, and a roughness length of 1 cm. The heat roughness length is 0.1 mm for the entire surface. The actual roughness lengths for heat and momentum of sea ice vary considerably depending on the surface state and degree or deformation due to wind and ocean forces; similarly, for water, these lengths depend on the wave field. The values we use here are characteristic of rough sea ice and wavy waters, but the conclusions and analyses on the effect of surface patterns will not be altered by a change in these surface properties.

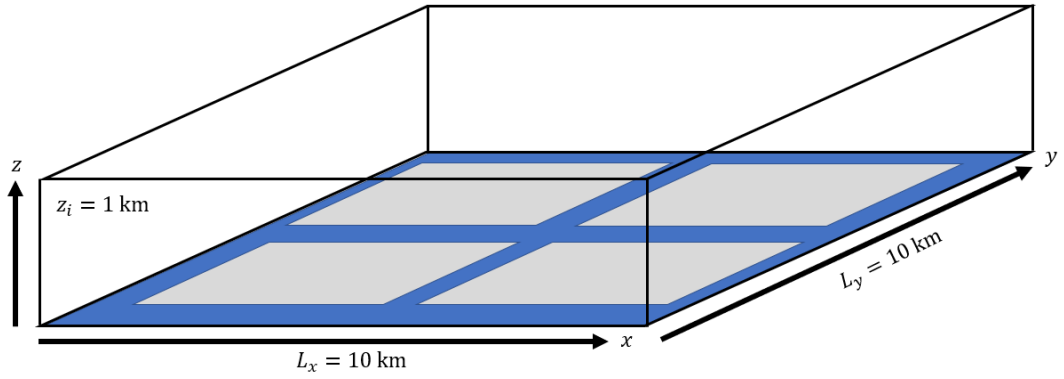

Figure 1. Schematic of the large-eddy simulation domain set-up. The ice (in grey) has a surface temperature of $\theta_{0,i} = 255\,\mathrm{K}$ and roughness length $z_{0,i} = 1\,\mathrm{mm}$; the water surface (in blue) has $\theta_{0,w} = 271\,\mathrm{K}$ and $z_{0,w} = 1\,\mathrm{cm}$. The bottom boundary represents one of the many cases (Pattern 1) illustrated in Figure 2.

This large-eddy simulation technique was used to simulate the MIZ-ABL over different idealized configurations of sea ice. All five patterns, displayed in figure 2, have a fixed sea ice fraction of $f_i = 0.46$ and mean floe area of $11.56 \times 10^6\,\mathrm{m}^2$. The geostrophic wind also flows left-to-right at an angle of $18°$ relative to the x-axis in all simulations, expected to give a surface wind that is roughly aligned with the x-axis for homogeneous neutral surfaces (Ghannam and Bou-Zeid, 2021). The turbulence field is warmed up for 60 hours, and the statistics are then Reynolds-averaged over an additional 12 hours. A variable with an overbar denotes averaging in time, used as a surrogate for ensemble Reynolds averaging, and any spatial averaging over the heterogeneous domain in x and y will be denoted by angled brackets.

2.2 Ice Map Data

While the LES utilizes idealized surfaces to examine the influence of patterns on the MIZ-ABL, examining what other landscape metrics might be important for surface characterization necessitates using real-world sea-ice maps. The lattice spatial data that will be used in the statistical analysis (see Section 2.3) are derived from recently declassified high-resolution (1 m) national technical means (NTM) literal image derived products (LIDPs), detailed in Kwok (2014). These images we use here had already underwent a supervised maximum likelihood classification algorithm, which assigned either a water or ice surface class (Fetterer and Untersteiner, 1998; Fetterer et al., 2008) for each pixel in the original LIDP. This process converted the

https://doi.org/10.5194/egusphere-2024-532
Preprint. Discussion started: 8 March 2024

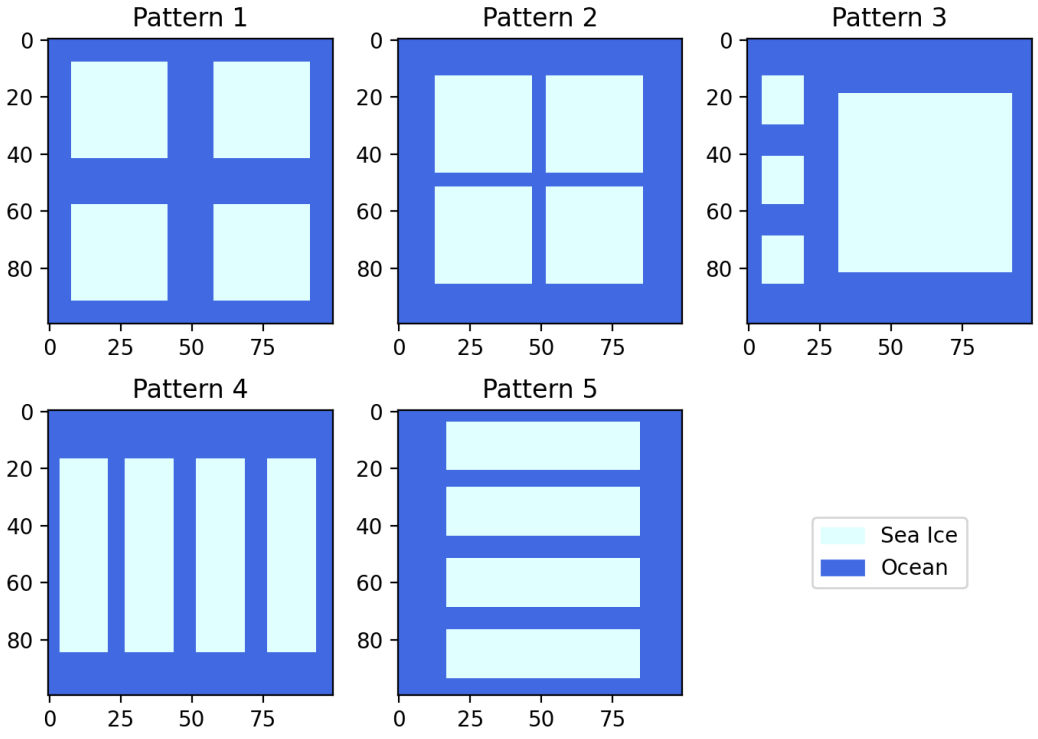

Figure 2. Birds-eye view of the bottom surfaces used in the large-eddy simulations. The geostrophic wind at the surface flows from left-to-right in all patterns.

high-resolution LIDPs into categorical lattice spatial data (where each cell represents one of two possible surface types, ice or water).

These maps, which have a horizontal extent of up to $10\,\mathrm{km}$ by $10\,\mathrm{km}$, comprise the dataset used to calculate landscape metrics. The advantage of this high-resolution large-extent data set is that we can analyze how these metrics change with grain size. These maps are thus aggregated from $1\,\mathrm{m}$ resolution to $2\,\mathrm{m}$, $10\,\mathrm{m}$, $20\,\mathrm{m}$, $50\,\mathrm{m}$, $100\,\mathrm{m}$, $200\,\mathrm{m}$, $500\,\mathrm{m}$, $1\,\mathrm{km}$, and $2\,\mathrm{km}$ resolutions; resampling was done using the nearest-neighbor method in the Python Imaging Library (PIL). These resolutions cover common resolutions used from fine large-eddy simulations to numerical weather prediction (NWP) models. Due to excessive computational processing time for the original $1\,\mathrm{m}$ resolution data, the highest resolution at which landscape metrics were calculated was $2\,\mathrm{m}$.

One important caveat of this dataset is that the histogram of sea ice fraction f_i is heavily skewed towards higher sea ice fractions. We recognize that this may lead to bias in the results; however, the analysis methods developed here are insensitive to f_i and can certainly be applied to other datasets with more uniform sea ice fraction distributions in the future. The high resolution afforded by the present dataset remains a key appealing factor in adopting it for the present study since it allows aggregating and tracking how landscape metrics change from actual surface states when resampled to a coarser numerical grid.

https://doi.org/10.5194/egusphere-2024-532
Preprint. Discussion started: 8 March 2024

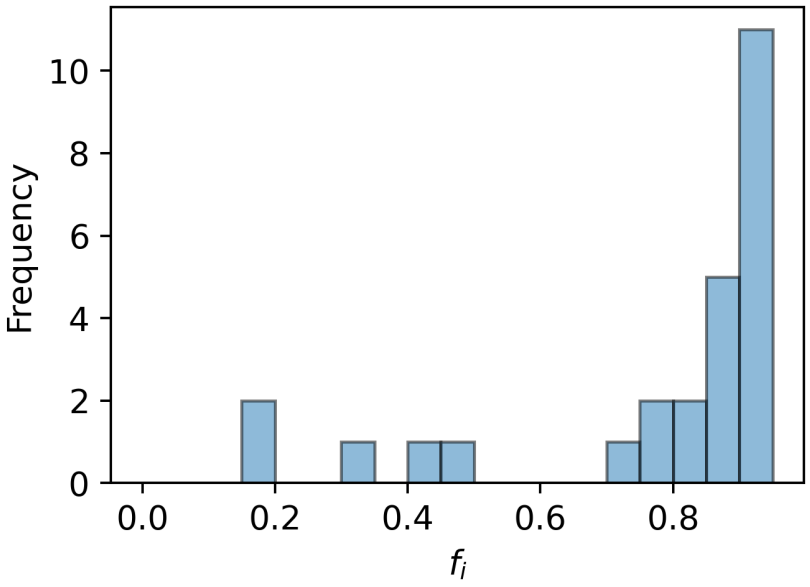

Figure 3. The distribution of f_i values in the Fetterer et al. (2008) ice map dataset

2.3 Landscape Metric Space Reduction

The FRAGSTATS spatial analysis program was used to calculate the landscape metrics (McGarigal and Marks, 1995) based off of lattice spatial data. Given a GeoTIFF-format raster lattice data, FRAGSTATS will calculate the patch metrics, class metrics, and landscape metrics of your choice. Patch metrics are computed for every patch in the landscape, and are thus not relevant for the current study of sea-ice surface patterns. Class metrics are computed for every patch type (class) in the landscape. In this study, that would mean calculating metrics for sea ice only and water only, which may be useful in other applications of pattern analysis, but for this study, we want to look at the aggregate patterns of sea ice and water combined. Thus, only landscape metrics were calculated. Sea ice fraction (calculated as the number of cells of ice type divided by the total number of ice and water cells) was calculated using PIL, the only metric not calculated by FRAGSTATS.

This resulted in 22 landscape metrics that focus on the global patterns of the surface. Many of these landscape metrics, however, are correlated with one another; for example, patch density and mean patch size are proportional to one another. This is due to the fact that there are limited observations one can make about a surface (number of patches, area of a patch, amount of edge in a patch, etc.), yet an infinite number of operations one can perform on them. Many of these metrics (especially at the landscape level) are thus simply different ways to aggregate or statistically analyze these observations.

While colinearity between two metrics can be easily detected through a correlation matrix, multicolinearity (when one indicator is a linear combination of two or more other indicators) is more likely in these types of data sets. It is thus possible for two or more landscape metrics to jointly define another metric. An objective and statistical way of reducing these parameters

https://doi.org/10.5194/egusphere-2024-532
Preprint. Discussion started: 8 March 2024

is hence needed. Here, we chose the variance inflation factor (VIF),

$$VIF_i = \frac{1}{1 - R_i^2}, \tag{1}$$

where R^2 is the coefficient of determination, to detect multicolinearity of these heterogeneity parameters (see Ibidoja et al. (2023)). For each metric X_i, where $i \in [1, ..., 22]$, the VIF was calculated over the regression equation

$$X_i = \alpha_0 + \alpha_{i+1} X_{i+1} + \alpha_{i+2} X_{i+2} + ... + \alpha_{21} X_{21} \tag{2}$$

where α_0 is a constant. The `statsmodels` Python library (Seabold and Perktold, 2010) was used for these computations. The metric with the largest VIF was then removed from the dataset, and thus not considered to be important in the quantification of sea ice surfaces. All VIFs were then recalculated for this 'reduced' dataset, and the new metric with the highest VIF was removed. Through this process, metrics are removed one by one until all remaining metrics exhibit a VIF less than a pre-defined cutoff, which was set as $VIF < 2.5$. While this low of a cutoff may not be necessary in certain practices of multicolinearity reduction (O'Brien, 2007), the ultimate goal of this technique is to reduce the parameter space. In other words, for climate modelers, a lower amount of metrics in their SGS parameterizations result in a more practical models.

Each of these metrics, listed in Table C1, can be clustered into one of six "metric groups": *Area and Edge*, *Shape*, *Core Area*, *Aggregation*, *Contrast*, and *Diversity*. The first four metrics are important in a sea ice surface. *Area and Edge* metrics deal with the size of floes and the amount of edge they create, while *Shape* metrics discriminate based on patch morphologies and overall geometric complexity. *Core Area* metrics analyze the area within a patch beyond some specified buffer width. An *Aggregation* metric will focus on the tendency of patches of similar types to be spatially aggregated in the landscape, or otherwise dispersed.

The last two metric groups, *Contrast* and *Diversity*, are less important for the present application to sea ice. *Contrast* metrics refers to the magnitude of difference between adjacent patch types with respect to some attribute - in the case of a sea ice surface, with only two classes (ice and ocean), there is only one 'contrast' between two categories, and thus metrics in this group are simply represented by the contrast of surface temperature and roughness. *Diversity* metrics are influenced by the number of patch types present and the area-weighted distribution of those patch types. In this case we only have two types of patches (ice and water) so the diversity is the same in all maps, and their weighted distribution is related to the ice fraction. Further information on all of these metric groups can be found in the FRAGSTATS manual (McGarigal and Marks, 1995).

3 Results: the MIZ-ABL over Idealized Configurations

The large-eddy simulation technique detailed in Section 2.1 was used to simulate the MIZ-ABL over different configurations of sea ice patterns, with the results presented here. Figure 4 displays the Reynolds- and horizontally-averaged normalized vertical profiles of the horizontal wind speed $M = \langle \sqrt{u^2 + v^2} \rangle$, total heat flux $\langle \overline{w\theta} \rangle$, and total horizontal stresses $\langle \overline{uw} \rangle$ and $\langle \overline{vw} \rangle$. Note that these lump the turbulent fluxes with the dispersive fluxes that arise over heterogeneous surfaces from the spatial correlation of the mean (time-averaged) fields (Raupach and Shaw, 1982; Finnigan and Shaw, 2008; Li and Bou-Zeid, 2019). The results clearly display significant differences, underlining the fact that sea ice fraction is not a sufficient surface metric to describe MIZ-ABL dynamics.

https://doi.org/10.5194/egusphere-2024-532
Preprint. Discussion started: 8 March 2024

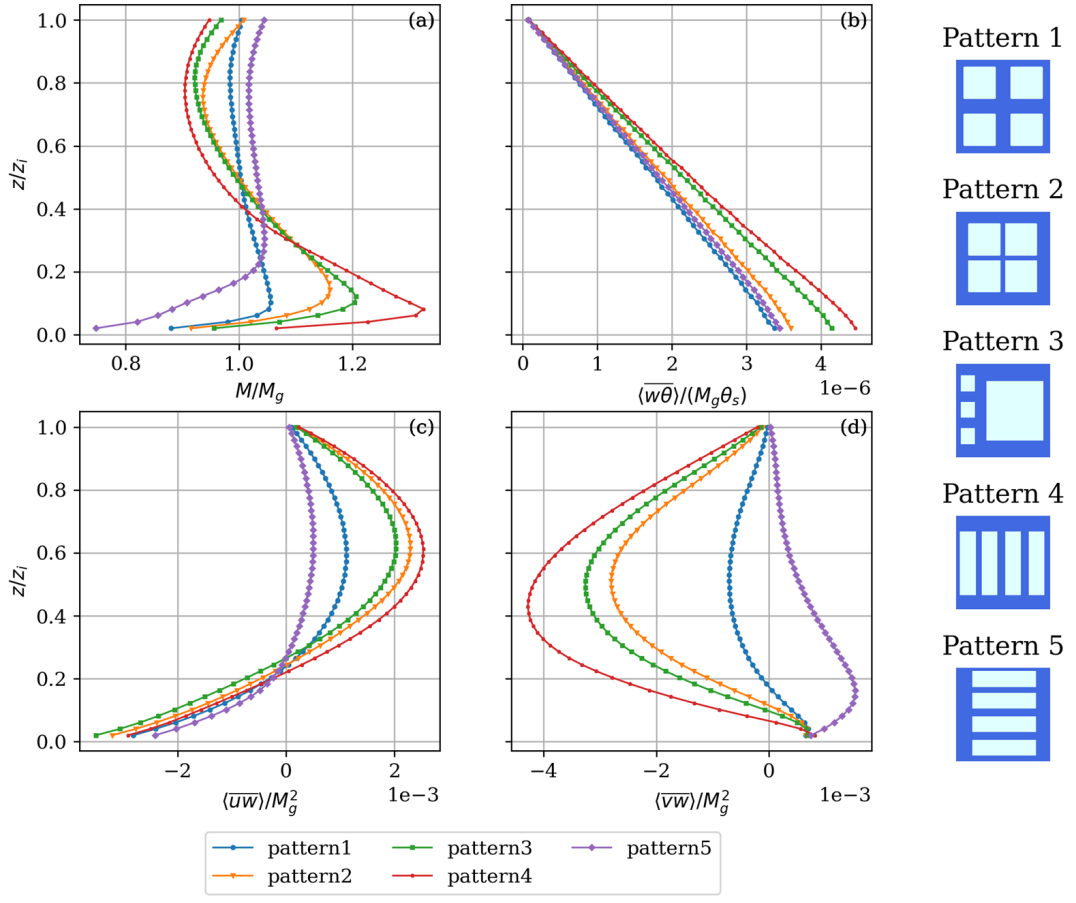

Figure 4. Vertical profiles of normalized (a) horizontal wind speed, (b) total heat flux, (c) total stress in the streamwise direction, and (d) total stress in the cross-stream direction, for all five patterns.

In all five simulations, the largest difference occurs between Pattern4 and Pattern5 (the red and purple lines, respectively), which is to be expected since the geostrophic wind is flowing parallel vs. perpendicular to the strips of ice (Willingham et al., 2014; Anderson et al., 2015; Salesky et al., 2022; Fogarty and Bou-Zeid, 2023). Although wind direction is not a surface property of the sea ice, its orientation relative to that of the surface features is still an important driver that must be taken into consideration and will be discussed further on. All patterns except for Pattern5 developed a low-level jet (LLJ), which can be seen in Figure 4a, though the LLJ in Pattern1 is remarkably weak. The LLJs seem to increase in Pattern2 and Pattern3, likely due to large swaths of ice in the direction of the geostrophic wind (and therefore little interruption by the unstable ocean surface). The second strongest LLJ is in Pattern3, and is likely due to the one large ice floe, and would persist for any wind direction (the same can be said about Pattern2). The strongest LLJ in Pattern4 is similarly explained by the secondary circulations (not shown) that consist of streamwise aligned rolls driven by the lateral contrast in surface temperature, and

https://doi.org/10.5194/egusphere-2024-532
Preprint. Discussion started: 8 March 2024

by the fact that the small strips of ocean between the ice floes are not wide enough to 'interrupt' the circulations and the geostrophic flow. However, unlike Pattern2 and Pattern3, Pattern4 is highly anisotropic, so the geostrophic wind direction is of more importance in this case, as can be deduced from the fact that Pattern5 has no LLJ despite being a 90° rotated version of Pattern4.

Major differences are also seen in the total streamwise and cross-stream stresses, displayed in Figure 4c and d, respectively. Again, Pattern4 and Pattern5 exhibit the highest differences from one another due to the geostrophic wind direction. All simulations have a similar negative streamwise stress in the surface layer, but at higher MIZ-ABL heights, the differences between simulations are greater. Above the LLJ, some of the stresses turn positive implying upward transfer of momentum from the LLJ, explaining differences that may be seen below the blending height (Wood and Mason, 1991; Mahrt, 2000; Brunsell et al., 2011). The cross-stream component of the total momentum flux, seen in 4d, are all quite distinct from one another indicating significant differences in the wind and stress Ekman rotation with height.

To further explain the differences seen in these patterns, we consider the decomposition of the total flux to its dispersive and turbulent counterparts. Vertical turbulent heat flux is designated as $\overline{w'\theta'}$, while vertical turbulent streamwise and cross-stream stress are designated as $\overline{u'w'}$, and $\overline{v'w'}$, respectively. Dispersive fluxes emerge in a time-averaged but spatially-variable mean flow (Raupach and Shaw, 1982; Li and Bou-Zeid, 2019). Since our Reynolds averaging is done in time, we can spatially decompose a Reynolds-averaged variable following $\overline{w} = \langle\overline{w}\rangle + \overline{w}''$, where the brackets represent the spatial average (as defined in Section 2.1) and the double-prime represents the variations of the mean planar fields in space. We then calculate the dispersive fluxes, using vertical heat flux as an example, by:

$$\overline{w}\overline{\theta} = \left(\langle\overline{w}\rangle + \overline{w}''\right)\left(\langle\overline{\theta}\rangle + \overline{\theta}''\right) \tag{3}$$

$$= \langle\overline{w}\rangle\langle\overline{\theta}\rangle + \overline{w}''\langle\overline{\theta}\rangle + \langle\overline{w}\rangle\overline{\theta}'' + \overline{w}''\overline{\theta}''. \tag{4}$$

We then spatially average the entirety of Equation 4 over the horizontal plane to obtain

$$\langle\overline{w}\overline{\theta}\rangle = \langle\overline{w}''\overline{\theta}''\rangle\,. \tag{5}$$

The middle two terms in Equation 4 are zero via spatial averaging, since $\langle\overline{w}''\rangle = 0$ and $\langle\overline{\theta}''\rangle = 0$ by definition; therefore, these terms have no impact on spatially-averaged surface-atmosphere exchanges. Furthermore, $\langle\overline{w}\rangle$ is assumed to be very small (unless strong and large scale subsidence or uplift are present); in our LES it must be zero since there cannot be accumulation or depletion of mass below a given horizontal plane in a periodic domain with an incompressible flow. Thus, the first term on the right hand side of Equation 4 is also negligible, leading to one remaining term in Equation 5. This term, the dispersive flux, is of most interest: it represents the coherent spatial correlation of vertical velocity and temperature in regions with consistent secondary structures (such as consistent warm updrafts or cool downdrafts, or streamwise rolls).

Figure 5 shows the vertical profiles of the total, turbulent, and dispersive horizontally-averaged fluxes of each pattern for the heat flux, streamwise momentum flux, and cross-stream momentum flux, thus allowing us to decompose and analyze the total fluxes that were shown in Figures 4b-d. For example, it is clearer now that the cross-stream components of the total momentum flux (Figure 4d) are all distinct from one another due to these dispersive fluxes (dotted green lines). Over these

https://doi.org/10.5194/egusphere-2024-532
Preprint. Discussion started: 8 March 2024

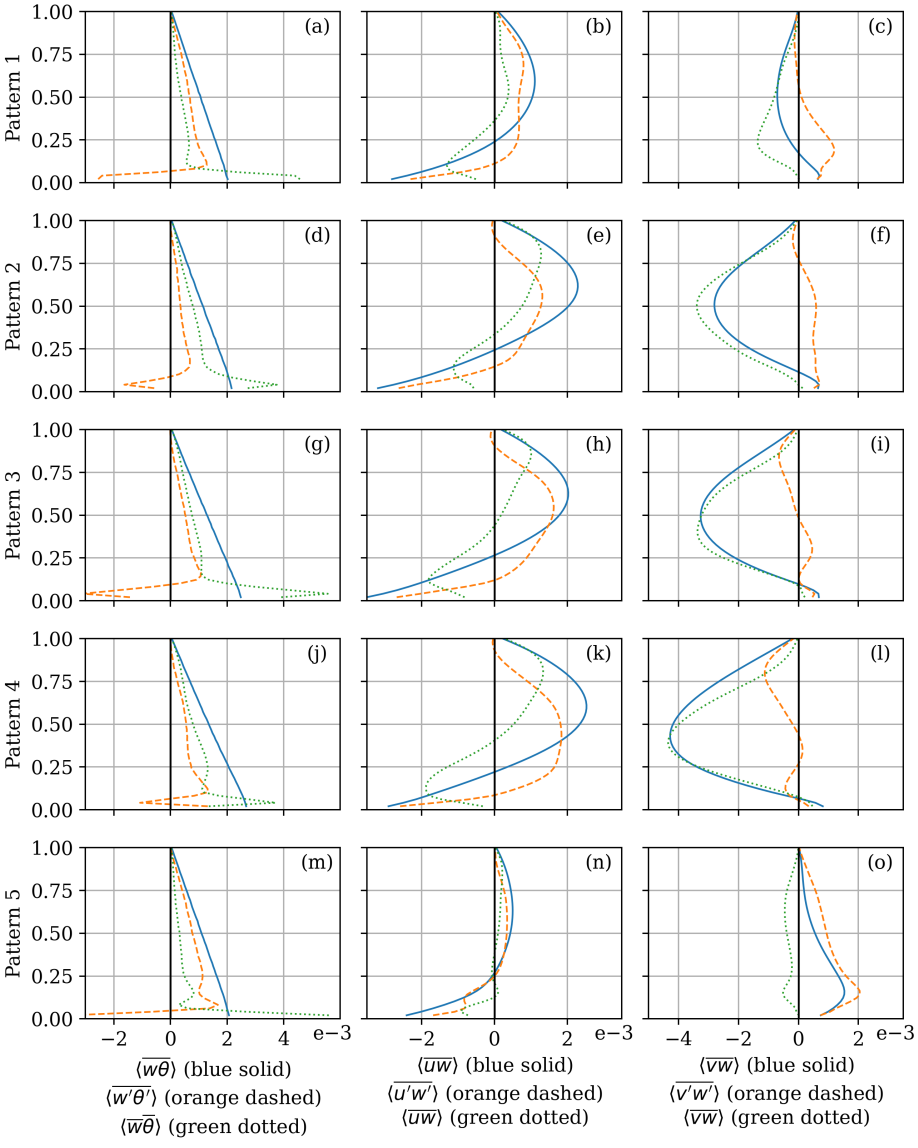

Figure 5. Left: Vertical profiles of normalized total heat flux ($\overline{w\theta}$, blue solid), turbulent heat flux ($\overline{w'\theta'}$, orange dashed), and dispersive heat flux ($\overline{\bar{w}\bar{\theta}}$, green dotted) for each individual pattern. Center: Same as left, but for normalized total streamwise stress ($\overline{uw}$, solid), turbulent streamwise stress ($\overline{u'w'}$, dashed), and dispersive streamwise stress ($\overline{\bar{u}\bar{w}}$, dotted). Right column: Same as left, but for normalized total cross-stream stress ($\overline{vw}$, solid), turbulent cross-stream stress ($\overline{v'w'}$, dashed), and dispersive cross-stream stress ($\overline{\bar{v}\bar{w}}$, dotted)

https://doi.org/10.5194/egusphere-2024-532
Preprint. Discussion started: 8 March 2024

Table 2. Dispersive-to-total atmospheric vertical flux ratios

	Pattern1	Pattern2	Pattern3	Pattern4	Pattern5
$\lvert\overline{\bar{w}\bar{\theta}}\rvert/\lvert\overline{w\theta}\rvert$	0.512	0.668	0.697	0.586	0.388
$\lvert\overline{\bar{u}\bar{w}}\rvert/\lvert\overline{uw}\rvert$	0.321	0.354	0.250	0.046	0.137
$\lvert\overline{\bar{v}\bar{w}}\rvert/\lvert\overline{vw}\rvert$	1.598	1.101	0.923	0.816	0.365

heterogeneous surfaces, the dispersive cross-stream stress is the dominant forcing in all patterns except Pattern5 (see panels c,f,i,l in Figure 5). The formation of these dispersive fluxes are not equal when the heterogeneous surfaces are different from one another. Thus it is not the ice fraction or average floe area, but the surface pattern itself, which leads to these differences in total cross-stream flux. The streamwise stresses, on the other hand, seem to be a balance of the dispersive and turbulent stresses that are not always of the same sign (middle column of Figure 5), and thus the dispersive components that directly result from the secondary motions imprinted by the surface pattern on the atmosphere are also critical here.

The total heat flux in all these simulations linearly decreases with height as dictated by the LES setup. As seen in Figure 4b, there are minimal differences in the total heat flux, except at the surface level; however, analyzing the left column of Figure 5 shows that the relative importance and profiles of the dispersive and turbulent heat fluxes exhibit more significant differences. The various surface patterns seem to lead to differences in the dispersive fluxes, but in all cases, these are balanced out by the turbulent fluxes. Nevertheless, in all the figures, there is strong variability near the surface in the dispersive and turbulent flux profiles. This is partially due to the shallow internal boundary layers that are created by the mean flow and secondary circulations over the floes, and it is these differing secondary circulations that arise due to the difference in surface pattern. However, one should also note that the first few points are also strongly influenced by the transition from the wall model to the SGS model in representing resolved turbulence, a persistent challenge in LES (Piomelli and Balaras, 2002; Brasseur and Wei, 2010); the quantitative details of the results in that region should be interpreted with care.

Lastly, analyzing the dispersive-to-total atmospheric vertical flux ratios (Table 2) lends insight into the differences between simulations, as well as comparison to other surface types. For example, in Pattern1 and Pattern2, $|\overline{\bar{v}\bar{w}}|/|\overline{vw}| > 1$, meaning that the dispersive and turbulent fluxes in the cross-stream axis are in opposite directions, which can be seen in the green and orange profiles in the right column in Figure 5c,f. The ratios in Pattern4 and Pattern5 are also closer to unity than the other values, again showing the differences in secondary circulations due to the sea ice pattern. These values have been seen before, for example over urban or forest canopies (Moltchanov et al., 2015; Boudreault et al., 2017; Li and Bou-Zeid, 2019).

Overall, these LES results indisputably indicate that ice-water patterns hold key information on how the MIZ-ABL interacts with the underlying surface, and the rest of the paper is thus dedicated to characterizing these patterns

4 Results: Statistical Analysis

Now that we have established the need for additional surface characteristics beyond sea ice fraction, we aim to examine what indicators can be used for that purpose. For each of the nine resolutions considered, there were 44 observed sea ice images

https://doi.org/10.5194/egusphere-2024-532
Preprint. Discussion started: 8 March 2024

analyzed. Conducting this analysis over the 2 m resolution, four metrics (including sea ice fraction) seemed to remain from the VIF elimination process and not exhibit multicolinearity with one another: sea ice fraction (f_i), patch density (PD), splitting index ($SPLIT$), and perimeter-area fractal dimension ($PAFRAC$). These remaining metrics were then grouped into the different metric groups defined in Section 2.3: the sea ice fraction is an *area and edge* metric, PD and $SPLIT$ are both *aggregation* metrics, while $PAFRAC$ is a *shape* metric. There were no metrics remaining that were in the *diversity*, *core area* or *contrast* metric group. We expected there to be no remaining metrics in the *contrast* metric group, since for a sea ice-water surface, an edge can only exhibit one "contrast" - however, this might change were this analysis to be conducted with continuously variable surface temperatures or roughness lengths. We also did not expect any in the *diversity* group, since many metrics such as evenness or Simpson's diversity index are functions of sea ice fraction. The absence of any representative of the *core area* was not predicted, but it is probably related to the fact that the *shape* and *area and edge* metrics are together able to represent the *core area* characteristics.

The first aggregation metric, PD (Riitters et al., 1995; Šímová and Gdulová, 2012), with a $VIF = 1.9$, is an area-normalized number of patches, described by the equation

$$PD = \frac{n}{A_t}, \tag{6}$$

where PD is the patch density, A_t the total area of the surface, and n the total number of distinct patches (of either sea ice or water). As the PD of a sea ice surface increases, one would expect to find more ice-water edge instances, and thus more regions of stable-to-unstable stratification transition. Patch density may also work in tandem with geostrophic wind direction, as discussed in Section 3, as a geostrophic wind flowing in one direction may have more ice-to-water edge transitions than another (see Pattern4 and Pattern5, for example).

The second metric, SPLIT, with a $VIF = 1.9$ was first described in Jaeger (2000) as "the probability that two randomly chosen places in a region will be found in the same undissected area," with a corresponding equation of

$$SPLIT = \frac{A_t^2}{\sum_{i=1}^{n} a_i^2} \tag{7}$$

where a_i is the area of patch i, and the index i iterates over all patches. $SPLIT = n$ if there is only one patch or if all patches are of equal size. However, generally $SPLIT < n$, with lower values indicating a larger variance in patch sizes. Since we already use PD, the new information $SPLIT$ brings is precisely about the patch size variance.

The only shape metric, $PAFRAC$, with a $VIF = 2.1$ is obtained by regressing each patch's perimeter P_i against its area A_i on a log-log plot such that

$$A = kP^{2/D}, \tag{8}$$

where k is a constant and D is the perimeter-area fractal dimension. It measures the tortuosity or jaggedness of the ice-water interface as with any fractal dimension (Mandelbrot, 1982).

Thus, the three metrics, in addition to sea ice fraction f_i, that would be useful in describing a sea-ice surface are $SPLIT$, PD, and $PAFRAC$. Table 3 details these values for each of the sea ice patterns simulated in Section 3. We observe that

https://doi.org/10.5194/egusphere-2024-532
Preprint. Discussion started: 8 March 2024

$SPLIT$ is invariant to the shape of floes as long as the area of each floe is equivalent (no variance), which is why $SPLIT$ is equivalent for all patterns except Pattern3. This is where $PAFRAC$ shows its utility, as it will give different values between Pattern1/Pattern2, Pattern3, and Pattern4/Pattern5.

Table 3. Landscape metrics of the simulations conducted in Section 3. Note that for maps with a low number of patches (less than ten) and/or simple shapes, PAFRAC may exceed the theoretical range, as in Pattern3, but this has not happened in any of the real sea ice maps we examine next.

Metric	**Pattern1**	**Pattern2**	**Pattern3**	**Pattern4**	**Pattern5**
f_i	0.462	0.462	0.461	0.462	0.462
Average Floe Area (m^2)	11.56×10^6	11.56×10^6	11.56×10^6	11.56×10^6	11.56×10^6
SPLIT	2.91	2.91	2.71	2.91	2.91
PD	5×10^{-8}	5×10^{-8}	5×10^{-8}	5×10^{-8}	5×10^{-8}
PAFRAC	1.895	1.895	2.035	1.929	1.929

In many cases, numerical simulations also require a resampling of the high-resolution surfaces by increasing the grain (pixel) size. For example, sea ice maps from reconnaissance satellites may have a resolution up to $1\,\mathrm{m}$, but this is computationally impractical for numerical weather models. Large-eddy simulations of the ABL can have up to a $50\,\mathrm{m}$ resolution, while NWP models have 2 to $5\,\mathrm{km}$ resolution. Thus, even with high-resolution data, the aggregation and resampling of these surface patterns is inevitable in modeling.

Therefore, it is useful to examine how these chosen metrics vary as an image is aggregated to a resolution applicable to numerical weather models (or other numerical models, such as LES). An appleaing metric would be one that it is invariant to a resolution change. The sea ice fraction f_i is a good example of such an invariant indicator, as shown in Figure 6a, where it is calculated for all images and then averaged over that resolution. A second-best case would be a metric that displays a clear scaling law with the resolution, such as PD depicted in Figure 6b. In this case, the PD for the "real" $2\,\mathrm{m}$ resolution surface can be extrapolated to higher resolutions based on a scaling power law

$$m = k\Delta^{D_q}\,, \tag{9}$$

where m is the metric, Δ is the map resolution, and k and D_q are scaling coefficients.

Some metrics, such as $SPLIT$ and $PAFRAC$ seems to exhibit close-to-invariant behavior after a sort of 'jump' in the resolution. For example, starting from the $10\,\mathrm{m}$ resolution, $SPLIT$ stays fairly constant as the resolution decreases. There is also variation in $PAFRAC$ as the resolution decreases from $10\,\mathrm{m}$. This is consistent with results from previous studies, as some landscape metrics exhibit large errors when these surfaces are aggregated to lower resolutions (Moody and Woodcock, 1994, 1995). Given the close-to-invariant scaling of 3 of the metrics and the predictable power law scaling of the forth, we can proceed with this set of 4 metrics since it is usable (or translatable) across scales.

https://doi.org/10.5194/egusphere-2024-532
Preprint. Discussion started: 8 March 2024

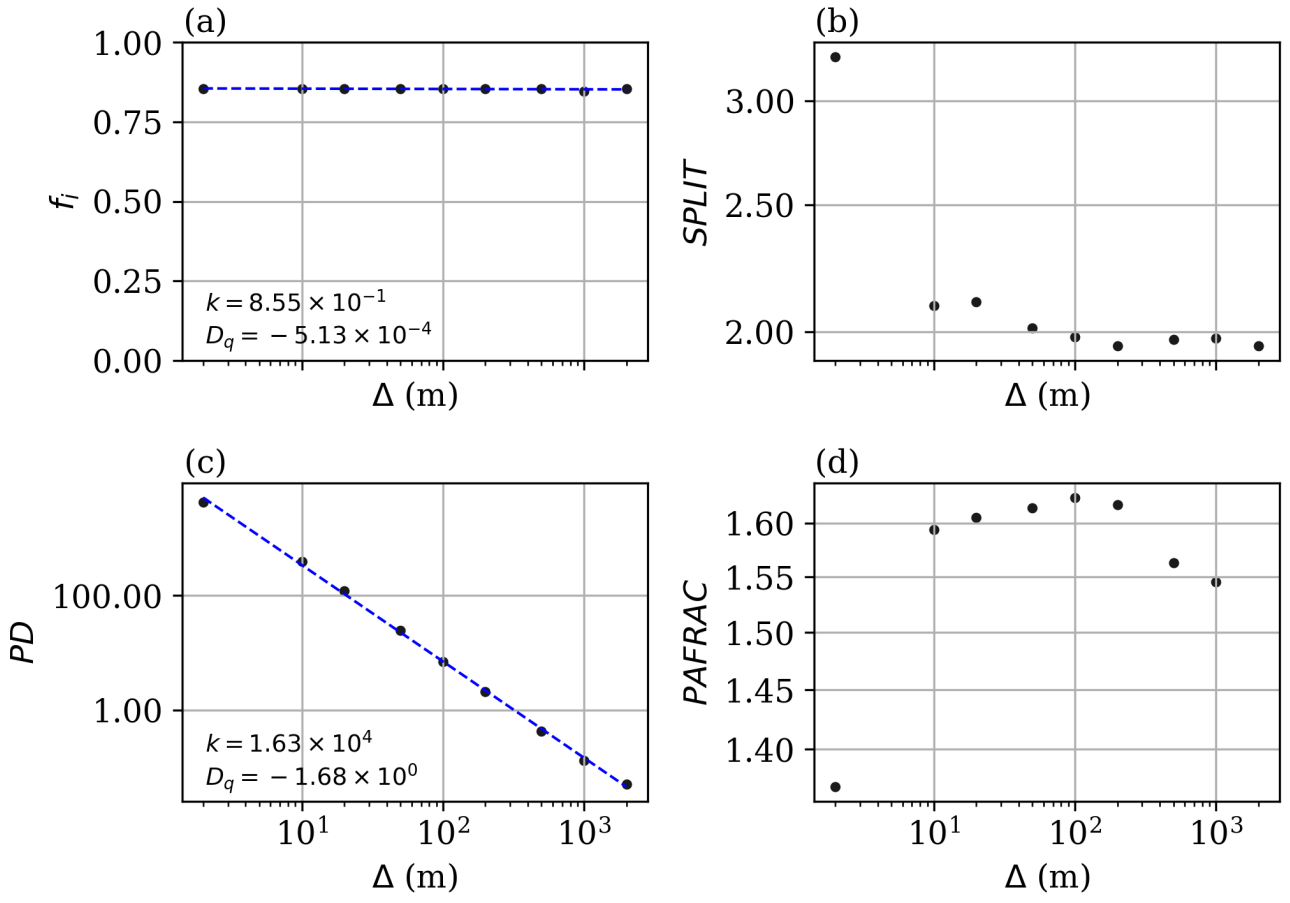

Figure 6. Landscape metric plotted against resolution for (a) sea ice fraction, (b) splitting index, (c) patch density, and (d) fractal dimension. A power law of the form $m = k\Delta^{D_q}$ is fitted to the sea ice fraction and patch density plots (dashed blue line), but no such power law is applicable to splitting index and fractal dimension.

https://doi.org/10.5194/egusphere-2024-532
Preprint. Discussion started: 8 March 2024

5 Principal Direction of Geostrophic Flow

Thus far, we have identified four surface pattern indicators that characterize the MIZ surface's sea ice versus water concentration (f_i), the density and thus the total number of patches (PD), the variance in the sizes of these patches ($SPLIT$), and the tortuosity of their edges $PAFRAC$. However re-examining Pattern4 and Pattern5 in Figure 4 raises the question as to why these maps have the largest differences in their respective MIZ-ABLs. Their geometric patterns are the same (thus the four metrics are identical for the two configurations), yet the difference in the geostrophic wind direction results in large differences in the surface-atmosphere interactions. This reveals that another important attribute is how the surface patterns are oriented relative to the wind. If the surface is isotropic, the wind angle should be irrelevant, but most water-sea ice patterns in the MIZ display a significant degree of anisotropy (Feltham, 2008). Therefore, quantifying the impact of surface orientation and including it in the metric set obtained from the VIF analysis in Section 4 may provide additional information for modelers to parameterize MIZ-ABL dynamics in global climate models.

We observe that in Pattern4 and Pattern5, the difference in the geostrophic direction is related to the directional variance of the data. In Pattern4, the wind is consistently blowing over an infinitely repeating pattern of sea ice and water at regular intervals. In Pattern5, the wind blows over much longer strips of ice and water, even though there are some sea ice-water transitions present. Any other oblique flow is thus "in between" these two 'parallel' and perpendicular regimes. We characterize the differences between these regimes by the variance of the surface that the surface wind is exposed to. In other words, Pattern4 exhibits a high variance (since over one domain length, the geostrophic wind flows over a maximum of eight ice-water transitions, and Pattern5 exhibits a low variance, since the geostrophic wind flows over a maximum of two sea ice-water transitions. This then raises the question of how to obtain some principal direction for a more complex surface.

We thus attempted to characterize this anisotropy by computing the direction of the eigenvector (the eigendirection) with the least amount of variance, thus giving the fewest ice-water transitions possible. This was done by implementing the *scikit-learn* Python package, via a principal component analysis (PCA) using the `sklearn.decomposition.PCA` class (Pedregosa et al., 2011). This method performs the eigendecomposition of the covariance matrix of our sea ice map, yielding two orthogonal eigenvectors. The principal eigendirection points in the direction of minimal variance, denoted by the longer of the two arrows in Figure 7. That is, the principle or most coherent mode that best explains the pattern is along the direction of least variability. The secondary eigendirection is, by definition, orthogonal to the principal eigenvector. Some of these eigendirections are intuitive, as one can 'imagine' trying to pick a geostrophic wind direction that passes over a minimal number of ice-water edges. The maps in Figures 7a and 7g are two such examples. However, the map in Figure 7f, for example, is a bit less intuitive - visual inspection may suggest that the principle eigendirection should aligned from the lower right to the upper left, but the results indicate a less obvious orientation.

It is hypothesized that for a fixed f_i, the geostrophic wind flowing in a principal direction with minimal variance will behave more so like Pattern5, and the perpendicular angle to that principal direction (the secondary direction) will behave more so like Pattern4 (similar to the parallel and perpendicular cases in the simulations conducted in Fogarty and Bou-Zeid (2023)),

https://doi.org/10.5194/egusphere-2024-532
Preprint. Discussion started: 8 March 2024

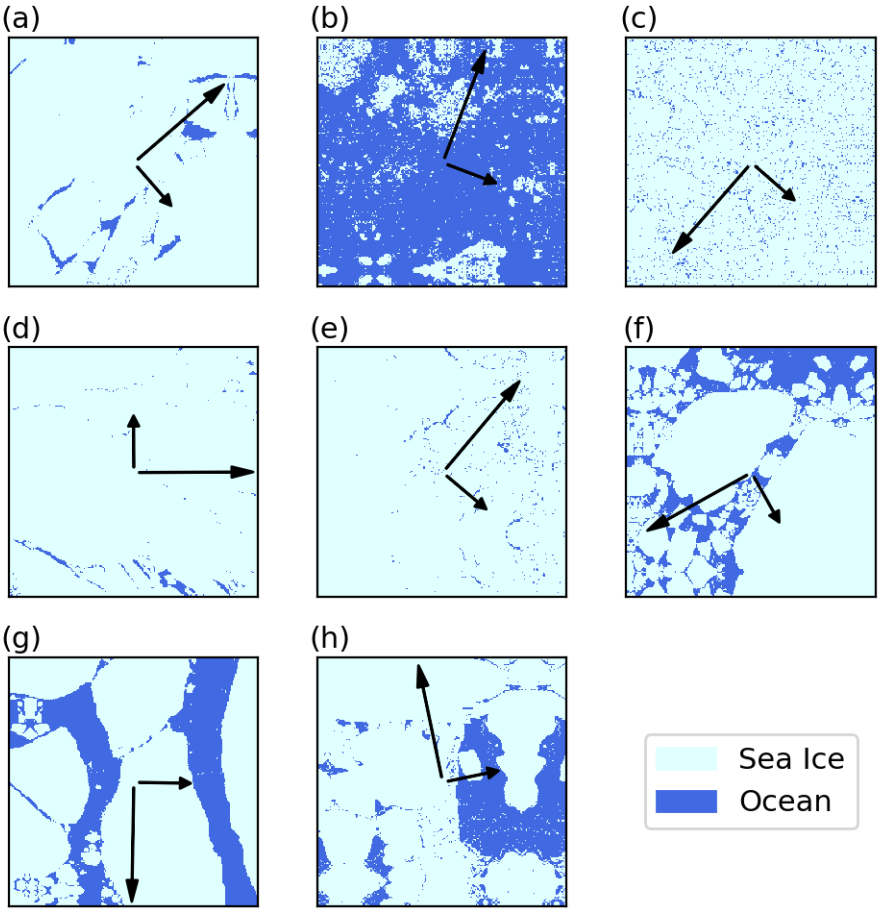

Figure 7. Eight maps from the sea ice dataset overlayed with their principal eigendirection (long arrow) and secondary eigendirection (short arrow), computed via principal-component analysis

but further LES simulations are needed to elucidate the exact impact of this relative orientation and the other parameters we identified on the MIZ-ABL.

However, some of these maps exhibit a higher degree of anisotropy than others, such as Figure 7c. To measure the degree of anisotropy in these maps, one may also look into percentage of variance (POV), defined as

$$\mathrm{POV}(\lambda_i) = \frac{\lambda_i}{\sum_{i=0}^{1} \lambda_i}, \tag{10}$$

for an eigenvector λ_i in an i-dimensional matrix. The POV of an eigenvector for a two-dimensional surface thus describes the amount of variance that can be explained (or reconstructed) by that eigenvector alone, such that $\lambda_0 + \lambda_1 = 1$. In theory, a sea ice map with a high $\mathrm{POV}(\lambda_0)$ would be anisotropic, since the principal eigendirection explains much more of the variance

https://doi.org/10.5194/egusphere-2024-532
Preprint. Discussion started: 8 March 2024

Table 4. Eigenvector (v_i) angle and eigenvalue (λ_i) for principal ($i = 0$) and secondary ($i = 1$) eigenvectors, as well as percentage of variance (POV) of λ_0, corresponding to each map in Figure 7. Note that these angles are not traditional meteorological wind angles, but are instead in Cartesian coordinates, as 0° is a left-to-right westerly wind

Map	$\angle v_0$	λ_0	$\angle v_1$	λ_1	POV(λ_0)
(a)	41°	3396	311°	3286	0.508
(b)	69°	4784	339°	2688	0.640
(c)	229°	3339	319°	3330	0.501
(d)	0°	3337	90°	3285	0.504
(e)	50°	3347	320°	3332	0.501
(f)	209°	3624	299°	2688	0.574
(g)	269°	3370	359°	3293	0.506
(h)	102°	3697	12°	3033	0.549

than the other mode, and the surface thus has a preferential direction of variability (one would expect Figure 7g to have a high POV(λ_0)). Conversely, a map with a low POV(λ_0) would be a fairly isotropic map.

By definition, POV(λ_0) > 0.5, since the POV(λ_0) is the POV for the principal eigendirection. However, most of the ratios in these examples lie in the range of $0.50 <$ POV(λ_0) < 0.60, showing little variability among these maps. Thus in this small subset of sea ice maps, solely looking at POV(λ_0) would not give information on how much influence the principal eigendirection has.

6 Conclusions

The ice fraction of a sea ice surface itself can be fair indicator of the behavior of the MIZ-ABL, if the ice fraction approaches 0.0 (all ocean, leading to an unstable atmosphere) or 1.0 (all ice, leading to a stable atmosphere). However, when the f_i is between these limits (in other words, if the surface flow alternates between very stable or very unstable), ice fraction alone is not enough to predict the dynamics and thermodynamics of the MIZ-ABL. Large-eddy simulations conducted for five different sea ice surfaces, detailed in Figure 2, have shown that surfaces with the same ice fraction, number of floes, and mean floe size can result in very distinct atmospheric dynamics. Differences were examined in the horizontal wind speed (Figure 4a) and total surface stresses (Figures 4c,d and 5).

While Figure 5 shows moderate differences in the total heat flux that is here constrained by the simulation setup, more significant differences are seen in the dispersive and turbulent fluxes that make up this flux (see also Table 2). The total, turbulent, and dispersive fluxes of the streamwise and cross-stream momentum were even more sensitive to the surface patterns. These dispersive fluxes are shown to drive many of the differences, and are thus non-negligible in climate models (Margairaz et al., 2020; Fogarty and Bou-Zeid, 2023; Lu et al., 2023).

https://doi.org/10.5194/egusphere-2024-532
Preprint. Discussion started: 8 March 2024

To understand what other information one can obtain from a two-dimensional binary lattice surface, we examined 44 spatial metrics traditionally used in the field of landscape ecology, since knowing the cover fraction (ice fraction), and the number and median area of the floes is not enough to fully describe the ice-water-atmosphere physics. These 44 additional spatial metrics were used on LIDPs of real-world satellite sea ice imagery to determine which metrics were important, and the variance inflation factor was used to detect and remove multicolinearity in this dataset. The remaining metric set included ice fraction, patch density (representing the number of sea ice floes and thus their mean size in a given total area), splitting index (representing the variance in the floe sizes) and the perimeter-area fractal dimension (representing edge tortuosity). We also propose the use of the surface eigendirection relative to the mean wind direction, to characterize the influence of surface anisotropy and its interaction with the wind direction.

The resulting five metric set, including eigendirection, is not only useful for describing a two-dimensional surface, but based on the VIF analysis, it is also a minimal set of indicators needed to describe such a surface since they contain distinct and important information. However, the development of practical parameterizations for sea ice and the MIZ-ABL will ultimately need to include additional considerations including the ease of obtaining these parameters for modeling applications, the computing time needed to calculate these surface metrics dynamically versus resolving the surface features when running an ESM, the availability of easier-to-compute surrogate metrics, among others.

The first step in answering this broad question is investigating to what degree these other metrics affect the MIZ-ABL, in comparison with the first-order effect on the MIZ-ABL of ice fraction. In other words, given an ice fraction, how will changing any of the metrics in the resulting set affect the overlying MIZ-ABL? While this was answered in this paper for idealized surfaces, proving that under some conditions these parameters are relevant, which of these parameters will be critical over real ice maps, and how often and to what degree, requires additional simulations (and is an underway followup to this study). More turbulence-resolving numerical simulations of the real ice surface are thus needed.

Another crucial step to answering this question is figuring out how one would go about creating an accurate parameterization based on the available external grid-cell variables; the resources to answer this question may be extensive as well. Again, even more large-eddy simulations, beyond what has been done here, over real sea ice maps are imperative to answer this question. Lastly, this open question also requires looking at how to incorporate the resulting metrics and eigendirections into these climate models, such as examining (i) how the geostrophic wind at certain principal directions interacts with the resulting metric set, (ii) other possible metrics of anisotropy, and (iii) how the sea ice model in an ESM can provide the data needed to capture the heterogeneity of the sea ice surface - among other questions that remain unanswered at this time.

Code and data availability. A dataset containing the simulation results for the five patterns, and the FRAGSTATS output for the sea ice maps, are publicly available at https://doi.org/10.34770/5x2y-5485. FRAGSTATS is publicly available for download/use at https://fragstats.org/ (McGarigal and Marks, 1995), and the prepossessed sea ice maps are available at Fetterer et al. (2008).

https://doi.org/10.5194/egusphere-2024-532
Preprint. Discussion started: 8 March 2024

Appendix A: Large-Eddy Simulation Details

In this study, the incompressible filtered Navier-Stokes equations (with the Boussinesq approximation for the mean state) and heat budget are solved for a horizontally periodic flow, where a variable with a tilde represents a quantity filtered via the numerical grid spacing Δ:

$$\frac{\partial \widetilde{u}_i}{\partial x_i} = 0 \,, \tag{A1}$$

$$\frac{\partial \widetilde{u}_i}{\partial t} + \widetilde{u}_j \frac{\partial \widetilde{u}_i}{\partial x_j} = -\frac{1}{\rho_r}\frac{\partial p}{\partial x_j} + \widetilde{F}_i + f_c \epsilon_{ij3} \widetilde{u}_j - g\delta_{i3}\left(1 - \frac{\hat{\theta}}{\theta_r}\right) - \frac{\partial \tau_{ij}}{\partial x_j} \,, \tag{A2}$$

$$\frac{\partial \widetilde{\theta}}{\partial t} + \widetilde{u}_j \frac{\partial \widetilde{\theta}}{\partial x_j} = -\frac{\partial q_j}{\partial x_j} \,. \tag{A3}$$

The equations above invoke the Einstein summation rule, where i is the free index and j the repeated index; u_i is the velocity vector; x_i is the position vector; p is a modified pressure (see Bou-Zeid et al. (2005) for details); θ is the potential temperature; θ_r and $\hat{\theta}$ are, respectively, the Boussinesq reference (planar mean in our calculations) and the perturbation from that reference for potential temperature; ρ_r is the reference mean density corresponding to θ_r; and F_i is the main flow-driving force (a synoptic pressure gradient). The Coriolis force is represented by the third term on the right-hand side of Eq.A2, where f_c is the Coriolis parameter and ϵ_{ij3} represents the Levi-Civita symbol. Buoyancy is represented by the fourth term on the right-hand side of Eq.A2, where δ_{ij} represents the Kronecker delta.

An overbar denotes averaging in time, used as a surrogate for ensemble Reynolds averaging, while spatial averaging over the heterogeneous domain (in both x and y) will be denoted by angled brackets. The sub-grid scale stress $\tau_{ij} = \widetilde{u_i u_j} - \widetilde{u}_i \widetilde{u}_j$ and buoyancy flux $q_j = \widetilde{u_j \theta} - \widetilde{u}_j \widetilde{\theta}$, which result from the filtering, are modelled using a Lagrangian scale-dependent dynamic model (Bou-Zeid et al., 2005) with a constant sub-grid scale Prandtl number of $\mathrm{Pr} = 0.4$. As noted before, the numerical grid is the inherent filter of the model, but any explicit filtering needed to compute the dynamic Smagorinsky constant c_s is done at scales 2Δ and 4Δ (2Δ for the local wall model); for these computations, a sharp-spectral cutoff filter is used. This model was validated by Bou-Zeid et al. (2005) for boundary layer flows over both homogeneous and heterogeneous terrain by reproducing experimental velocity and stress profiles obtained by Bradley (1968) after a change in surface roughness. It was then further validated for urban flows (Tseng et al., 2006; Li et al., 2016), and both stable and unstable boundary layers (Kleissl et al., 2006; Kumar et al., 2006; Huang and Bou-Zeid, 2013). Therefore, the ability of this model to successfully capture the impacts of stability and spatial transitions in surface properties was not tested further in this paper.

The LES employs boundary conditions that are periodic in the horizontal, with zero vertical velocity at the top and bottom of the domain, as well as a stress-free top lid ($\partial_z u_i = 0$ where $i = 1, 2$), with zero heat flux. These mimic a very strong top inversion, and are adequate for our setup since the top of the domain is not stably stratified and there is thus no need for a sponge to avoid wave reflection. This allows for the surface characteristics to be isolated from z_i and the inversion strength. The indices $i = 1, 2, 3$ represent the x, y, and z directions, oriented along the streamwise, cross-stream, and vertical directions, respectively. At the bottom of the domain, the surface stress and heat flux are computed by a wall model based on a local law-of-the-wall formulation (Bou-Zeid et al., 2005), with Monin-Obukhov buoyancy correction. Numerically, a pseudo-spectral approach is

https://doi.org/10.5194/egusphere-2024-532
Preprint. Discussion started: 8 March 2024

employed in the horizontal, and an explicit second-order centred difference scheme used in the vertical. Time advancement is done using the fully explicit second-order Adams-Bashforth scheme. Dealiasing of the convective terms is performed using the 3/2 rule (Orszag, 1971). Pressure is computed from a Poisson equation obtained by taking divergence of the momentum equation and applying the incompressibility assumption.

Appendix B: Temperature Initialization

The initial temperature was chosen to be one such that the heat flux over the ice is equivalent to the heat flux coming from the water, based on the area fraction (ice fraction, in this case) of the of the domain. Thus, the initial air temperature of the large-eddy simulation was chosen such that the ice-fraction weighted heat flux over the ice ($f_i H_i$) was equivalent to the water fraction weighted heat flux over the ocean ($f_w H_w$),

$$-f_i H_i = f_w H_w \,, \tag{B1}$$

where $f_i + f_w = 1$. Using Monin-Obukhov flux profiles relations to express the surface fluxes:

$$\theta_i - \theta_a = \frac{H_i}{\kappa u_{*,i} \rho c_p} \left[\ln\left(\frac{z}{z_{0h,i}}\right) - \Psi_s\left(\frac{z}{L_i}\right) \right], \tag{B2}$$

$$\theta_w - \theta_a = \frac{H_w}{\kappa u_{*,w} \rho c_p} \left[\ln\left(\frac{z}{z_{0h,w}}\right) - \Psi_u\left(\frac{z}{L_w}\right) \right], \tag{B3}$$

where θ_a is the bulk air temperature; θ_i is the temperature of the ice surface; θ_w is the temperature of the ocean surface; $\kappa \approx 0.4$ is the von Kármán constant; $u_{*,i}$ and $u_{*,i}$ are the friction velocities of the ice and water surface respectively; ρ is the density of air; c_p is the specific heat of air; z is a height near the surface (taken at $z = 50\,\mathrm{m}$); $z_{0h,i}$ and $z_{0h,w}$ are the scalar roughness lengths of the ice and water surface, respectively; L_i and L_w are the Obukhov lengths over the ice and water surface respectively; and Ψ_s and Ψ_u represent the stable and unstable correction functions, respectively, as reported in Brutsaert (2005). These Obukhov lengths are defined as

$$L_i = \frac{-u_{*,i}^3 \rho c_p}{H_i \kappa (g/\theta_a)}, \tag{B4}$$

$$L_w = \frac{-u_{*,w}^3 \rho c_p}{H_w \kappa (g/\theta_a)}, \tag{B5}$$

where the value of H_i and H_w in these equations is taken as a first-order estimate obtained by rearranging Equations B2 and B3 without the stability functions (i.e., for a neutral atmosphere),

$$H_i = (\theta_i - \theta_a) \kappa u_{*,i} \left(\ln \frac{z}{z_{0h,i}} \right)^{-1}, \tag{B6}$$

$$H_w = (\theta_w - \theta_a) \kappa u_{*,w} \left(\ln \frac{z}{z_{0h,w}} \right)^{-1}, \tag{B7}$$

which allows one to write a function substituting Equations B2 and B3 into Equation B1 to obtain a function that can be solved for θ_a via numerical root-finding. Of course, this is only a first guess to initialize the LES, which will then dynamically create its air temperature field during the warm-up period.

https://doi.org/10.5194/egusphere-2024-532
Preprint. Discussion started: 8 March 2024

Appendix C: Landscape Quantification Metrics

Table C1 lists the landscape metrics used in the VIF analysis conducted in Section 4. For more information on each individual metric (other than ice fraction), consult the FRAGSTATS manual (McGarigal and Marks, 1995).

Table C1. All landscape metrics used in the VIF analysis conducted in Section 4

Ice Fraction	Edge Density	Interspersion and Juxtaposition Index
Number of Patches	Landscape Shape Index	Patch Cohesion Index
Patch Density	Perimeter-Area Fractal Dimension	Landscape Division Index
Largest Patch Index	Contagion Index	Effective Mesh Size
Total Edge	Percentage of Like Adjacencies	Splitting Index
Modified Simpson Evenness Index	Aggregation Index	Shannon Diversity Index
Simpson Diversity Index	Modified Simpson Diversity Index	Shannon Eveness Index
Simpson Evenness Index		

Author contributions. Joseph Fogarty: Conceptualization, Methodology, Formal analysis, Investigation, Writing - Original Draft, Visualization. Elie Bou-Zeid: Methodology, Investigation, Formal analysis, Writing - Review and Editing, Supervision, Funding acquisition. Mitchell Bushuk: Writing - Review and Editing, Validation. Linette Boisvert: Writing - Review and Editing, Validation. All authors reviewed the results and approved the final version of the manuscript.

Competing interests. No competing interests are present.

Acknowledgements. This research was supported by the US National Science Foundation under award number AGS 2128345 and the National Oceanic and Atmospheric Administration, U.S. Department of Commerce under by award NA18OAR4320123. The statements, findings, conclusions, and recommendations are those of the authors and do not necessarily reflect the views of the National Oceanic and Atmospheric Administration, or the U.S. Department of Commerce. We would also like to acknowledge high-performance computing support from Cheyenne (Computational and Information Systems Laboratory, 2019) provided by NCAR's Computational and Information Systems Laboratory, sponsored by the National Science Foundation, under projects UPRI0007 and UPRI0021.

https://doi.org/10.5194/egusphere-2024-532
Preprint. Discussion started: 8 March 2024

References

Allouche, M., Katul, G. G., Fuentes, J. D., and Bou-Zeid, E.: Probability law of turbulent kinetic energy in the atmospheric surface layer, Physical Review Fluids, 6, 074 601, https://doi.org/10.1103/PhysRevFluids.6.074601, 2021.

Allouche, M., Bou-Zeid, E., and Iipponen, J.: The Influence of Synoptic Wind on Land-Sea Breezes, Quarterly Journal of the Royal Meteorological Society, n/a, https://doi.org/10.1002/qj.4552, 2023.

Anderson, W., Barros, J. M., Christensen, K. T., and Awasthi, A.: Numerical and experimental study of mechanisms responsible for turbulent secondary flows in boundary layer flows over spanwise heterogeneous roughness, Journal of Fluid Mechanics, 768, 316–347, https://doi.org/10.1017/jfm.2015.91, 2015.

Baidya Roy, S.: Impact of land use/land cover change on regional hydrometeorology in Amazonia, J. Geophys. Res., 107, 8037, https://doi.org/10.1029/2000JD000266, 2002.

Bates, N. R., Moran, S. B., Hansell, D. A., and Mathis, J. T.: An increasing CO2 sink in the Arctic Ocean due to sea-ice loss, Geophysical Research Letters, 33, https://doi.org/10.1029/2006gl027028, 2006.

Bou-Zeid, E., Meneveau, C., and Parlange, M. B.: Large-eddy simulation of neutral atmospheric boundary layer flow over heterogeneous surfaces: Blending height and effective surface roughness: LES OF NEUTRAL ATMOSPHERIC BOUNDARY LAYER FLOW, Water Resour. Res., 40, https://doi.org/10.1029/2003WR002475, 2004.

Bou-Zeid, E., Meneveau, C., and Parlange, M.: A scale-dependent Lagrangian dynamic model for large eddy simulation of complex turbulent flows, Physics of Fluids, 17, 025 105, https://doi.org/10.1063/1.1839152, 2005.

Bou-Zeid, E., Parlange, M. B., and Meneveau, C.: On the Parameterization of Surface Roughness at Regional Scales, Journal of the Atmospheric Sciences, 64, 216–227, https://doi.org/10.1175/JAS3826.1, 2007.

Bou-Zeid, E., Anderson, W., Katul, G. G., and Mahrt, L.: The Persistent Challenge of Surface Heterogeneity in Boundary-Layer Meteorology: A Review, Boundary-Layer Meteorol, 177, 227–245, https://doi.org/10.1007/s10546-020-00551-8, 2020.

Boudreault, L.-, Dupont, S., Bechmann, A., and Dellwik, E.: How Forest Inhomogeneities Affect the Edge Flow, Boundary-Layer Meteorology, 162, 375–400, https://doi.org/10.1007/s10546-016-0202-5, 2017.

Bourassa, M. A., Gille, S. T., Bitz, C., Carlson, D., Cerovecki, I., Clayson, C. A., Cronin, M. F., Drennan, W. M., Fairall, C. W., Hoffman, R. N., Magnusdottir, G., Pinker, R. T., Renfrew, I. A., Serreze, M., Speer, K., Talley, L. D., and Wick, G. A.: High-Latitude Ocean and Sea Ice Surface Fluxes: Challenges for Climate Research, Bulletin of the American Meteorological Society, 94, 403 – 423, https://doi.org/10.1175/BAMS-D-11-00244.1, 2013.

Bradley, E. F.: A micrometeorological study of velocity profiles and surface drag in the region modified by a change in surface roughness, Q.J Royal Met. Soc., 94, 361–379, https://doi.org/10.1002/qj.49709440111, 1968.

Brasseur, J. G. and Wei, T.: Designing large-eddy simulation of the turbulent boundary layer to capture law-of-the-wall scaling, Physics of Fluids, 22, 1–21, https://doi.org/10.1063/1.3319073, 2010.

Brunsell, N. A., Mechem, D. B., and Anderson, M. C.: Surface heterogeneity impacts on boundary layer dynamics via energy balance partitioning, Atmospheric Chemistry and Physics, 11, 3403–3416, https://doi.org/10.5194/acp-11-3403-2011, 2011.

Brutsaert, W.: Hydrology: An Introduction, Cambridge University Press, https://doi.org/10.1017/CBO9780511808470, 2005.

Casagrande, F., Stachelski, L., and De Souza, R. B.: Assessment of Antarctic sea ice area and concentration in Coupled Model Intercomparison Project Phase 5 and Phase 6 models, International Journal of Climatology, 43, 1314–1332, https://doi.org/10.1002/joc.7916, 2023.

https://doi.org/10.5194/egusphere-2024-532
Preprint. Discussion started: 8 March 2024

Computational and Information Systems Laboratory: Cheyenne: HPE/SGI ICE XA System (University Community Computing). Boulder, CO: National Center for Atmospheric Research, https://doi.org/10.5065/D6RX99HX, 2019.

Courault, D., Drobinski, P., Brunet, Y., Lacarrere, P., and Talbot, C.: Impact of surface heterogeneity on a buoyancy-driven convective boundary layer in light winds, Boundary-Layer Meteorol, 124, 383–403, https://doi.org/10.1007/s10546-007-9172-y, 2007.

Cressie, N.: Statistics for Spatial Data - Revised Edition, Wiley Series in Probability and Statistics, John Wiley & Sons, Inc., https://doi.org/10.1002/9781119115151, 1993.

Crosman, E. T. and Horel, J. D.: Sea and lake breezes: A review of numerical studies, Boundary-layer meteorology, 137, 1–29, 2010.

Cushman, S. A., McGarigal, K., and Neel, M. C.: Parsimony in landscape metrics: Strength, universality, and consistency, Ecological Indicators, 8, 691–703, https://doi.org/10.1016/j.ecolind.2007.12.002, 2008.

de Vrese, P., Schulz, J.-P., and Hagemann, S.: On the Representation of Heterogeneity in Land-Surface–Atmosphere Coupling, Boundary-Layer Meteorology, 160, 157–183, https://doi.org/10.1007/s10546-016-0133-1, 2016.

Docquier, D. and Koenigk, T.: Observation-based selection of climate models projects Arctic ice-free summers around 2035, Communications Earth & Environment, 2, 144, https://doi.org/10.1038/s43247-021-00214-7, 2021.

Dumont, D.: Marginal ice zone dynamics: history, definitions and research perspectives, Philosophical Transactions of the Royal Society A: Mathematical, Physical and Engineering Sciences, 380, 20210 253, https://doi.org/10.1098/rsta.2021.0253, 2022.

Esau, I. N.: Amplification of turbulent exchange over wide Arctic leads: Large-eddy simulation study, Journal of Geophysical Research: Atmospheres, 112, https://doi.org/10.1029/2006jd007225, 2007.

Essery, R. L. H., Best, M. J., Betts, R. A., Cox, P. M., and Taylor, C. M.: Explicit Representation of Subgrid Heterogeneity in a GCM Land Surface Scheme, Journal of Hydrometeorology, 4, 530 – 543, https://doi.org/10.1175/1525-7541(2003)004<0530:EROSHI>2.0.CO;2, 2003.

Feltham, D. L.: Sea Ice Rheology, Annual Review of Fluid Mechanics, 40, 91–112, https://doi.org/10.1146/annurev.fluid.40.111406.102151, 2008.

Fetterer, F. and Untersteiner, N.: Observations of melt ponds on Arctic sea ice, J. Geophys. Res., 103, 24 821–24 835, https://doi.org/10.1029/98JC02034, 1998.

Fetterer, F., Wilds, S., and Sloan., J.: Arctic Sea Ice Melt Pond Statistics and Maps, 1999-2001, Version 1, https://doi.org/10.7265/N5PK0D32, 2008.

Finnigan, J. J. and Shaw, R. H.: Double-averaging methodology and its application to turbulent flow in and above vegetation canopies, Acta Geophysica, 56, 534–561, https://doi.org/10.2478/s11600-008-0034-x, 2008.

Fogarty, J. and Bou-Zeid, E.: The Atmospheric Boundary Layer Above the Marginal Ice Zone: Scaling, Surface Fluxes, and Secondary Circulations, Boundary-Layer Meteorology, https://doi.org/10.1007/s10546-023-00825-x, 2023.

Ghannam, K. and Bou-Zeid, E.: Baroclinicity and directional shear explain departures from the logarithmic wind profile, QJR Meteorol. Soc, 147, 443–464, https://doi.org/10.1002/qj.3927, 2021.

Herman, A., Wenta, M., and Cheng, S.: Sizes and Shapes of Sea Ice Floes Broken by Waves–A Case Study From the East Antarctic Coast, Frontiers in Earth Science, 9, 655 977, https://doi.org/10.3389/feart.2021.655977, 2021.

Horvat, C.: Marginal ice zone fraction benchmarks sea ice and climate model skill, Nature Communications, 12, 2221, https://doi.org/10.1038/s41467-021-22004-7, 2021.

https://doi.org/10.5194/egusphere-2024-532
Preprint. Discussion started: 8 March 2024

Huang, H.-Y., Margulis, S. A., Chu, C. R., and Tsai, H.-C.: Investigation of the impacts of vegetation distribution and evaporative cooling on synthetic urban daytime climate using a coupled LES-LSM model, Hydrol. Process., 25, 1574–1586, https://doi.org/10.1002/hyp.7919, 2011.

Huang, J. and Bou-Zeid, E.: Turbulence and Vertical Fluxes in the Stable Atmospheric Boundary Layer. Part I: A Large-Eddy Simulation Study, Journal of the Atmospheric Sciences, 70, 1513–1527, https://doi.org/10.1175/JAS-D-12-0167.1, 2013.

Hwang, B. and Wang, Y.: Multi-scale satellite observations of Arctic sea ice: new insight into the life cycle of the floe size distribution, Philosophical Transactions of the Royal Society A: Mathematical, Physical and Engineering Sciences, 380, 20210259, https://doi.org/10.1098/rsta.2021.0259, 2022.

Ibidoja, O. J., Shan, F. P., Sulaiman, J., and Ali, M. K. M.: Detecting heterogeneity parameters and hybrid models for precision farming, Journal of Big Data, 10, 130, https://doi.org/10.1186/s40537-023-00810-8, 2023.

Jaeger, J. A.: Landscape division, splitting index, and effective mesh size: new measures of landscape fragmentation, Landscape Ecology, 15, 115–130, https://doi.org/10.1023/A:1008129329289, 2000.

Kleissl, J., Kumar, V., Meneveau, C., and Parlange, M. B.: Numerical study of dynamic Smagorinsky models in large-eddy simulation of the atmospheric boundary layer: Validation in stable and unstable conditions, Water Resources Research, 42, https://doi.org/10.1029/2005WR004685, 2006.

Kumar, V., Kleissl, J., Meneveau, C., and Parlange, M. B.: Large-eddy simulation of a diurnal cycle of the atmospheric boundary layer: Atmospheric stability and scaling issues: LES OF A DIURNAL CYCLE OF THE ABL, Water Resour. Res., 42, https://doi.org/10.1029/2005WR004651, 2006.

Kwok, R.: Declassified high-resolution visible imagery for Arctic sea ice investigations: An overview, Remote Sensing of Environment, 142, 44–56, https://doi.org/10.1016/j.rse.2013.11.015, 2014.

Li, H. and Reynolds, J. F.: A Simulation Experiment to Quantify Spatial Heterogeneity in Categorical Maps, Ecology, 75, 2446, https://doi.org/10.2307/1940898, 1994.

Li, H. and Reynolds, J. F.: On Definition and Quantification of Heterogeneity, Oikos, 73, 280, https://doi.org/10.2307/3545921, 1995.

Li, Q. and Bou-Zeid, E.: Contrasts between momentum and scalar transport over very rough surfaces, J. Fluid Mech., 880, 32–58, https://doi.org/10.1017/jfm.2019.687, 2019.

Li, Q., Bou-Zeid, E., Anderson, W., Grimmond, S., and Hultmark, M.: Quality and reliability of LES of convective scalar transfer at high Reynolds numbers, International Journal of Heat and Mass Transfer, 102, 959–970, https://doi.org/10.1016/j.ijheatmasstransfer.2016.06.093, 2016.

Liu, C., Yang, Y., Liao, X., Cao, N., Liu, J., Ou, N., Allan, R. P., Jin, L., Chen, N., and Zheng, R.: Discrepancies in Simulated Ocean Net Surface Heat Fluxes over the North Atlantic, Advances in Atmospheric Sciences, 39, 1941–1955, https://doi.org/10.1007/s00376-022-1360-7, 2022.

Lu, J., Nazarian, N., Hart, M. A., Krayenhoff, E. S., and Martilli, A.: Representing the effects of building height variability on urban canopy flow, Quarterly Journal of the Royal Meteorological Society, n/a, https://doi.org/10.1002/qj.4584, 2023.

Mahrt, L.: Surface heterogeneity and vertical structure of the boundary layer, Boundary-Layer Meteorology, 96, 33–62, 2000.

Mandelbrot, B.: How Long Is the Coast of Britain? Statistical Self-Similarity and Fractional Dimension, Science, 156, 636–638, https://doi.org/10.1126/science.156.3775.636, 1967.

Mandelbrot, B. B.: The fractal geometry of nature, Freeman, San Francisco, CA, https://cds.cern.ch/record/98509, 1982.

https://doi.org/10.5194/egusphere-2024-532
Preprint. Discussion started: 8 March 2024

Margairaz, F., Pardyjak, E. R., and Calaf, M.: Surface Thermal Heterogeneities and the Atmospheric Boundary Layer: The Relevance of Dispersive Fluxes, Boundary-Layer Meteorology, 175, 369–395, https://doi.org/10.1007/s10546-020-00509-w, 2020.

Maronga, B. and Raasch, S.: Large-Eddy Simulations of Surface Heterogeneity Effects on the Convective Boundary Layer During the LITFASS-2003 Experiment, Boundary-Layer Meteorol, 146, 17–44, https://doi.org/10.1007/s10546-012-9748-z, 2013.

McGarigal, K. and Marks, B. J.: FRAGSTATS: spatial pattern analysis program for quantifying landscape structure., Tech. Rep. PNW-GTR-351, U.S. Department of Agriculture, Forest Service, Pacific Northwest Research Station, Portland, OR, https://doi.org/10.2737/PNW-GTR-351, 1995.

Michaelis, J., Lüpkes, C., Zhou, X., Gryschka, M., and Gryanik, V. M.: Influence of Lead width on the Turbulent Flow Over Sea Ice Leads: Modeling and Parametrization, Journal of Geophysical Research: Atmospheres, 125, https://doi.org/10.1029/2019JD031996, cited by: 6; All Open Access, Green Open Access, Hybrid Gold Open Access, 2020.

Miles, J.: Tolerance and Variance Inflation Factor, John Wiley & Sons, Ltd, https://doi.org/https://doi.org/10.1002/9781118445112.stat06593, 2014.

Miller, N. B., Shupe, M. D., Cox, C. J., Noone, D., Persson, P. O. G., and Steffen, K.: Surface energy budget responses to radiative forcing at Summit, Greenland, The Cryosphere, 11, 497–516, https://doi.org/10.5194/tc-11-497-2017, 2017.

Moltchanov, S., Bohbot-Raviv, Y., Duman, T., and Shavit, U.: Canopy edge flow: A momentum balance analysis, Water Resources Research, 51, 2081–2095, https://doi.org/https://doi.org/10.1002/2014WR015397, 2015.

Momen, M. and Bou-Zeid, E.: Large-Eddy Simulations and Damped-Oscillator Models of the Unsteady Ekman Boundary Layer*, Journal of the Atmospheric Sciences, 73, 25–40, https://doi.org/10.1175/JAS-D-15-0038.1, 2016.

Moody, A. and Woodcock, C.: Scale-dependent errors in the estimation of land-cover proportions: Implications for global land-cover datasets, Photogrammetric engineering and remote sensing, 60, 585–594, 1994.

Moody, A. and Woodcock, C. E.: The influence of scale and the spatial characteristics of landscapes on land-cover mapping using remote sensing, Landscape Ecol, 10, 363–379, https://doi.org/10.1007/BF00130213, 1995.

Myksvoll, M. S., Britt Sandø, A., Tjiputra, J., Samuelsen, A., Çağlar Yumruktepe, V., Li, C., Mousing, E. A., Bettencourt, J. P., and Ottersen, G.: Key physical processes and their model representation for projecting climate impacts on subarctic Atlantic net primary production: A synthesis, Progress in Oceanography, 217, 103 084, https://doi.org/10.1016/j.pocean.2023.103084, 2023.

Nilsson, E. D., Rannik, , Swietlicki, E., Leck, C., Aalto, P. P., Zhou, J., and Norman, M.: Turbulent aerosol fluxes over the Arctic Ocean: 2. Wind-driven sources from the sea, Journal of Geophysical Research: Atmospheres, 106, 32 139–32 154, https://doi.org/https://doi.org/10.1029/2000JD900747, 2001.

Notz, D. and Community, S.: Arctic Sea Ice in CMIP6, Geophysical Research Letters, 47, e2019GL086 749, https://doi.org/https://doi.org/10.1029/2019GL086749, e2019GL086749 10.1029/2019GL086749, 2020.

Notz, D. and Stroeve, J.: The Trajectory Towards a Seasonally Ice-Free Arctic Ocean, Current Climate Change Reports, 4, 407–416, https://doi.org/10.1007/s40641-018-0113-2, 2018.

Orszag, S. A.: On the Elimination of Aliasing in Finite-Difference Schemes by Filtering High-Wavenumber Components, Journal of the Atmospheric Sciences, 28, 1074, 1971.

O'Brien, R. M.: A Caution Regarding Rules of Thumb for Variance Inflation Factors, Quality & Quantity, 41, 673–690, https://doi.org/10.1007/s11135-006-9018-6, 2007.

https://doi.org/10.5194/egusphere-2024-532
Preprint. Discussion started: 8 March 2024

Pedregosa, F., Varoquaux, G., Gramfort, A., Michel, V., Thirion, B., Grisel, O., Blondel, M., Prettenhofer, P., Weiss, R., Dubourg, V., Vanderplas, J., Passos, A., Cournapeau, D., Brucher, M., Perrot, M., and Duchesnay, E.: Scikit-learn: Machine Learning in Python, Journal of Machine Learning Research, 12, 2825–2830, 2011.

Persson, P. O. G., Fairall, C. W., Andreas, E. L., Guest, P. S., and Perovich, D. K.: Measurements near the Atmospheric Surface Flux Group tower at SHEBA: Near-surface conditions and surface energy budget, Journal of Geophysical Research: Oceans, 107, SHE 21–1–SHE 21–35, https://doi.org/https://doi.org/10.1029/2000JC000705, 2002.

Pickett, S. T. A. and Cadenasso, M. L.: Landscape Ecology: Spatial Heterogeneity in Ecological Systems, Science, 269, 331–334, https://doi.org/10.1126/science.269.5222.331, 1995.

Piomelli, U. and Balaras, E.: Wall-Layer Models for Large-Eddy Simulations, Annual Review of Fluid Mechanics, 34, 349–374, https://doi.org/10.1146/annurev.fluid.34.082901.144919, 2002.

Porson, A., Steyn, D. G., and Schayes, G.: Sea-breeze scaling from numerical model simulations, part II: Interaction between the sea breeze and slope flows, Boundary-layer meteorology, 122, 31–41, 2007.

Ramudu, E., Gelderloos, R., Yang, D., Meneveau, C., and Gnanadesikan, A.: Large Eddy Simulation of Heat Entrainment Under Arctic Sea Ice, Journal of Geophysical Research: Oceans, 123, 287–304, https://doi.org/10.1002/2017jc013267, 2018.

Raupach, M. R. and Shaw, R. H.: Averaging Procedures for Flow Within Vegetation Canopies, Boundary-Layer Meteorology, 22, 79–90, https://doi.org/10.1007/BF00128057, 1982.

Ren, H., Zhang, C., and Zhao, X.: Numerical simulations on the fracture of a sea ice floe induced by waves, Applied Ocean Research, 108, 102 527, https://doi.org/https://doi.org/10.1016/j.apor.2021.102527, 2021.

Riitters, K. H., O'Neill, R. V., Hunsaker, C. T., Wickham, J. D., Yankee, D. H., Timmins, S. P., Jones, K. B., and Jackson, B. L.: A factor analysis of landscape pattern and structure metrics, Landscape Ecol, 10, 23–39, https://doi.org/10.1007/BF00158551, 1995.

Rosenblum, E. and Eisenman, I.: Faster Arctic Sea Ice Retreat in CMIP5 than in CMIP3 due to Volcanoes, J. Climate, 29, 9179–9188, https://doi.org/10.1175/JCLI-D-16-0391.1, 2016.

Rosenblum, E. and Eisenman, I.: Sea Ice Trends in Climate Models Only Accurate in Runs with Biased Global Warming, Journal of Climate, 30, 6265–6278, https://doi.org/10.1175/JCLI-D-16-0455.1, 2017.

Salesky, S. T., Calaf, M., and Anderson, W.: Unstable turbulent channel flow response to spanwise-heterogeneous heat fluxes: Prandtl's secondary flow of the third kind, Journal of Fluid Mechanics, 934, A46, https://doi.org/10.1017/jfm.2022.15, 2022.

Seabold, S. and Perktold, J.: statsmodels: Econometric and statistical modeling with python, in: 9th Python in Science Conference, 2010.

Stoll, R., Gibbs, J. A., Salesky, S. T., Anderson, W., and Calaf, M.: Large-Eddy Simulation of the Atmospheric Boundary Layer, Boundary-Layer Meteorol, 177, 541–581, https://doi.org/10.1007/s10546-020-00556-3, 2020.

Stroeve, J., Holland, M. M., Meier, W., Scambos, T., and Serreze, M.: Arctic sea ice decline: Faster than forecast, Geophysical Research Letters, 34, https://doi.org/10.1029/2007GL029703, 2007.

Strong, C., Foster, D., Cherkaev, E., Eisenman, I., and Golden, K. M.: On the Definition of Marginal Ice Zone Width, J. Atmos. Oceanic Technol., 34, 1565–1584, https://doi.org/10.1175/JTECH-D-16-0171.1, 2017.

Taylor, P. C., Hegyi, B. M., Boeke, R. C., and Boisvert, L. N.: On the Increasing Importance of Air-Sea Exchanges in a Thawing Arctic: A Review, Atmosphere, 9, https://doi.org/10.3390/atmos9020041, 2018.

Tseng, Y.-H., Meneveau, C., and Parlange, M. B.: Modeling Flow around Bluff Bodies and Predicting Urban Dispersion Using Large Eddy Simulation, Environ. Sci. Technol., 40, 2653–2662, https://doi.org/10.1021/es051708m, 2006.

https://doi.org/10.5194/egusphere-2024-532
Preprint. Discussion started: 8 March 2024

Wang, Y., Holt, B., Erick Rogers, W., Thomson, J., and Shen, H. H.: Wind and wave influences on sea ice floe size and leads in the B eaufort and C hukchi S eas during the summer-fall transition 2014, Journal of Geophysical Research: Oceans, 121, 1502–1525, https://doi.org/10.1002/2015JC011349, 2016.

Wenta, M. and Herman, A.: The influence of the spatial distribution of leads and ice floes on the atmospheric boundary layer over fragmented sea ice, Ann. Glaciol., 59, 213–230, https://doi.org/10.1017/aog.2018.15, 2018.

Wenta, M. and Herman, A.: Area-Averaged Surface Moisture Flux over Fragmented Sea Ice: Floe Size Distribution Effects and the Associated Convection Structure within the Atmospheric Boundary Layer, Atmosphere, 10, 654, https://doi.org/10.3390/atmos10110654, 2019.

Willingham, D., Anderson, W., Christensen, K. T., and Barros, J. M.: Turbulent boundary layer flow over transverse aerodynamic roughness transitions: Induced mixing and flow characterization, Physics of Fluids, 26, 025 111, https://doi.org/10.1063/1.4864105, 2014.

Wood, N. and Mason, P.: The influence of static stability on the effective roughness lengths for momentum and heat transfer, Quarterly Journal of the Royal Meteorological Society, 117, 1025–1056, https://doi.org/https://doi.org/10.1002/qj.49711750108, 1991.

Šímová, P. and Gdulová, K.: Landscape indices behavior: A review of scale effects, Applied Geography, 34, 385–394, https://doi.org/https://doi.org/10.1016/j.apgeog.2012.01.003, 2012.